Journal of
*Marine Science and Engineering*

MDPI

*Article*

# Effects of Slotted Blades on the Hydrodynamic Performance of Horizontal Axis Tidal Turbines

**Guangyong Yang [1], Zhaoyong Mao [1,2,3], Tianqi Zhang [2] and Wenlong Tian [2,3,*]**

[1] Unmanned System Research Institute, Northwestern Polytechnical University, Xi'an 710072, China; yangguangyong@mail.nwpu.edu.cn (G.Y.)
[2] School of Marine Science and Technology, Northwestern Polytechnical University, Xi'an 710072, China
[3] Key Laboratory for Unmanned Underwater Vehicle, Northwestern Polytechnical University, Xi'an 710072, China
* Correspondence: tianwenlong@nwpu.edu.cn; Tel.: +86-8849-5250

**Abstract:** The horizontal axis tidal turbine (HATT) is a device that harnesses the energy of ocean currents and converts it into electrical energy. The blade plays a crucial role in the efficiency of power generation in HATTs. This study focuses on the use of slotted blades to enhance the efficiency of HATTs and investigates the flow control mechanism of these slots using computational fluid dynamics (CFD) methods. Initially, CFD simulations were conducted to analyze the impact of the slot's geometry parameters on a two-dimensional (2-D) slot and to demonstrate its passive fluid control mechanism. Subsequently, the slot was implemented on three-dimensional (3-D) blades to examine its effect on the hydrodynamic performance of the blades. The results of the 2-D simulation indicate that the width and position of the slots have a significant influence on the lift-to-drag ratio of the hydrofoils, resulting in a maximum increase of 166%. For the 3-D blades, the simulation results reveal that the slot can enhance the power coefficient of the blades, particularly at low tip-speed ratios, with a maximum increase of 7.8%.

**Keywords:** tidal energy; passive flow control; slotted blades; horizontal axis tidal turbines; numerical simulation

check for updates

**Citation:** Yang, G.; Mao, Z.; Zhang, T.; Tian, W. Effects of Slotted Blades on the Hydrodynamic Performance of Horizontal Axis Tidal Turbines. *J. Mar. Sci. Eng.* **2023**, *11*, 1545. https://doi.org/10.3390/jmse11081545

Academic Editor: Kamal Djidjeli

Received: 6 July 2023
Revised: 28 July 2023
Accepted: 30 July 2023
Published: 3 August 2023



## 1. Introduction

It is widely accepted that nuclear and renewable energy will be more widely used in the future [1,2], that clean and renewable energy will play a prominent role, and that the global trend is towards more renewable energy [3,4]. Ocean current energy is widely studied as a crucial renewable energy source [5]. The global ocean current energy capacity is vast, with a projected total of 120 GW [6]. In general, ocean current energy can be captured by vertical and horizontal axis turbines [7]. Horizontal axis tidal turbines (HATTs) are widely used in the development of ocean current energy due to their high operational efficiency [8] and are considered to be the most promising among various ocean current energy devices [9]. Significant advances in horizontal axis turbine technology have been made in recent years with the deployment of pre-commercial-stage megawatt-scale units (e.g., Hammerfest Strøm HS1000 [10], Simek Atlantis AR1500 [11], Orbital Ocean's $O_2$ [12]).

The blade is a critical component of the HATTs, and its performance has a direct impact on the efficiency of the turbine's power generation. Flow separation often occurs at the root of the HATT blades, resulting in a significant reduction in lift and a decrease in the blade power coefficient, which restricts the performance of the turbine. Flow control has the potential to significantly enhance the hydrodynamic efficiency of blades, such as through the implementation of active jetting [13,14]. The utilization of passive flow control on HATT blades is highly popular due to its ability to enhance performance without requiring any additional energy [15].

The slot extending from the pressure side of the airfoil/hydrofoil to the suction side is applied to the airfoil/hydrofoil. Due to the pressure difference between the two sides, a jet is formed in the slot from the pressure surface to the suction surface. The boundary layer on the upper surface is injected with fluid momentum, causing the flow separation to be delayed. Yavuz et al. [16] performed a three-dimensional analysis of the two hydrofoil-slot arrangements and found that both arrangements can improve efficiency within certain limits. Wei et al. [17] conducted a numerical study on the hydraulic and cavitation characteristics of a slotted hydrofoil at the angle of incidence of 6°. The numerical results indicate that the optimized slotted hydrofoil has better hydraulic and cavitation performance. Liu et al. [18] applied slots on hydrofoils to suppress cavitation instability, and simulated and compared cavitation behavior and drag/lift forces to study the impact of slot geometry on cavitation suppression. Belamadi et al. [19] investigated the effect of slots on the airfoil and found that the slot improved the performance of the blade when the angle of attack was larger. Moshfeghi et al. [20] and Xie et al. [21] also studied the influence of slots on the S809 airfoil. Beyhaghi et al. [22] studied the effect of slots installed on the leading edge of the NACA 4412 airfoil on its performance, and the results showed that slots can increase the average lift coefficient of the wing by up to 7%, while the drag coefficient remained unchanged. Kundu [23] studied the impact of the slot on the S1210 airfoil, and the results showed that the slot delayed the stall angle of the airfoil, and the slot starting from the leading edge could improve the performance of the airfoil. Ni et al. [24,25] studied the effects of a new type of slot and showed that the maximum lift coefficient and maximum lift-to-drag ratio of the slot hydrofoil were both improved. Mohamed et al. [26] conducted a numerical study on wind turbine blades with slots, and the results showed that the flow separation on the slotted airfoil was delayed and the optimal lift-to-drag ratio of the slotted airfoil covered a more extensive range of angle of attack. Abolfazl et al. [27] used a three-dimensional numerical simulation method to accurately analyze the aerodynamic performance of wind turbines with varying configurations of slotted blades. The results indicated that the slotted airfoil achieved a significant improvement in the average torque coefficient.

Research on the flow field characteristics and hydrodynamic performance of predicted HATTs has been of great interest, and much research has been carried out regarding numerical calculations and experimental tests. The RANS (Reynolds Averaged Navier–Stokes) method is the most common in the numerical computation of the HATT flow field, and the turbulence model generally uses benchmark models such as k-ε and k-ω. Tian et al. [28] analyzed the effect of yaw angle and turbulence intensity on the performance of a 20 kW flow-powered turbine by using three-dimensional transient CFD simulations, and the results showed that Cp and Ct decrease with increasing yaw angle. Tian et al. [29] carried out a wake interference simulation by the RANS method using an actuator disk model instead of a turbine. Bahaj et al. [30] measured the effect of different tip-speed ratios and pitch settings on power and thrust coefficients in a cavitation tunnel and a towing tank. Kolekar et al. [31] investigated the effect of flow Reynolds numbers and solid blockage on turbine performance through experimental and computational studies. Badshah et al. [32] investigated the effect of blockage ratio on HATT performance using the SST k-ω turbulence model. Amiri et al. [33] used a k-ε turbulence model combined with a multi-reference frame (MRF) to design, study, and optimize horizontal axis tidal turbines, and validated the simulation results using AeroDyn BEM code. Lee et al. [34] investigated the effect of counter-rotating blade spacing on the hydrodynamic performance of HATTs using a k-ω turbulence model combined with an MRF. Liu et al. [35] compared the prediction performance of HATTs based on the RANS method with both slip-grid and MRF approaches, and found that the slip-grid method was more accurate for predicting wake flow. Sánchez et al. [36,37] optimized the horizontal axis wind turbine parameters to maximize efficiency using the Python programming language. In terms of experimental studies, Chen et al. [38] conducted a careful experimental analysis of HATT wake propagation in a circulating water channel, and the results showed that the blocking of the rotor and struts caused a reduction in the wake velocity. Mycek et al. [39] investigated the influence of the distribution of the incoming turbulence intensity of tandem turbines using towing tank tests. Yamini et al. [40] explored scenarios for avoiding or solving hydraulic problems using hydraulic modeling studies, and discussed the formation of vortices at the entrance. Zhang et al. [41] experimentally investigated the wake thrust characteristics of two-rotor HATTs through a circulating water channel. In this paper, the CFD method combined with the MRF is used to predict the hydrodynamic performance of HATTs.

There have been many studies that have clarified the importance of slots in improving hydrofoil performance. Most of the research on the effect of slots on blade performance has been based on 2-D foils. However, for tidal turbine blades, the angle of attack and the Reynolds number are different for each cross-section, and, in addition, the radial flow of the blade cannot be neglected. Therefore, the influence of the slot on the 3-D blades needs to be considered separately. Moshfeghi et al. [42] studied the effect of slots on 3-D blades, but they chose only two slots in different configurations.

In this research, a novel slot design is proposed, where the exit of the slot is tangent to the upper surface of the hydrofoil and is applied to the turbine blade. The main objective of this proposed slot shape is to accelerate the jet and enhance the control of induced flow, ultimately leading to improved hydrofoil performance. Numerical simulations demonstrate that this new design significantly enhances the effectiveness of slot-induced flow control, surpassing previous slot designs at low tip-speed ratios. Furthermore, this paper examines the flow control mechanism of the slot and comprehensively evaluates the effects of various geometric parameters on slotted blades, aiming to determine the optimal configuration.

The findings of this study hold great significance for enhancing the efficiency of power generation in tidal energy turbines. By extending the effectiveness of the slot, this research contributes to the progress and wider adoption of tidal current energy, aligning with the objectives of sustainable development.

## 2. Geometric Description

This study involved a fixed-pitch, three-blade turbine with a diameter of 1.2 m [43]. The hydrofoils used by this blade are interpolated according to the fx77-w-121, fx77-w-153, and fx77-w-258 hydrofoils [44]. The turbine is designed for a flow velocity of 0.5 m/s and a designed optimum tip-speed ratio of 5; the flow Reynolds number on three-dimensional blades ranges from $2 \times 10^4$ to $3.5 \times 10^5$. The special slot, whose exit is tangent to the hydrofoils, is applied to the 3-D blades, as shown in Figure 1 [25]. The influence of parameters such as the exit position of the slot in the chord direction, the exit width, and the applied length in the blade elongation direction on the blade were considered.

To facilitate subsequent analysis, the following dimensionless parameters are introduced.

Lift coefficient:

$$C_L = L/(0.5\rho {V_\infty}^2 S) \tag{1}$$

Drag coefficient:

$$C_D = D_1/(0.5\rho {V_\infty}^2 S) \tag{2}$$

Pressure coefficient:

$$Cpressure = (p - p_\infty)/(0.5\rho {V_\infty}^2) \tag{3}$$

Tip-speed ratio:

$$TSR = \omega R_b/V_0 \tag{4}$$

Thrust coefficient:

$$C_T = T/(0.5\rho\pi {R_b}^2 {V_0}^2) \tag{5}$$

Power coefficient:

$$C_P = M\omega/(0.5\rho\pi {R_b}^2 {V_0}^3) \tag{6}$$

Among these, $L$ is the lift on the hydrofoil; $D_1$ is the drag force; $S$ is the reference area of the hydrofoil; $p$ is the pressure on the hydrofoil; $p_\infty$ is the far-field pressure; $T$ is the turbine thrust; $M$ is the turbine torque.

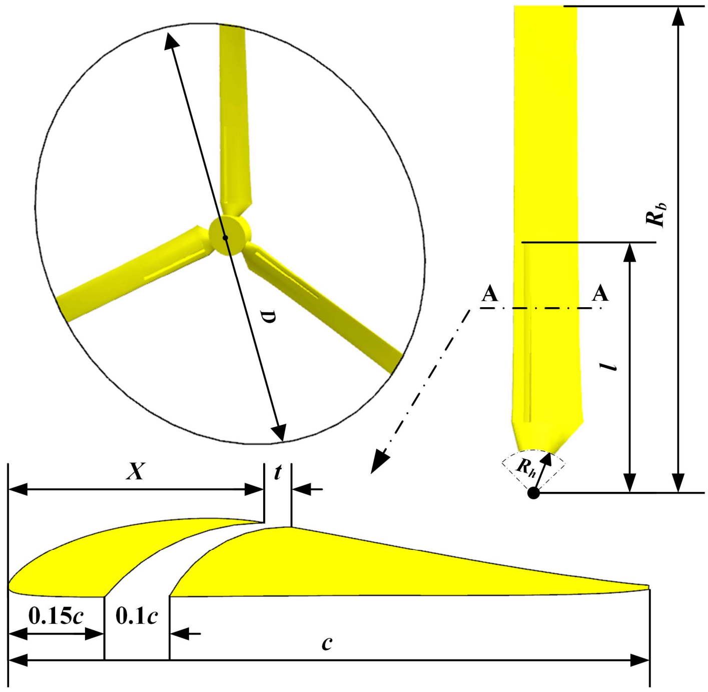


**Figure 1.** Rotor with slotted blades.

## 3. Simulation Model

### 3.1. Basic Equations

The governing equations for this study are represented by the Reynolds Averaged Navier–Stokes (RANS) equations. These equations encompass the continuity and momentum equations, which are expressed as follows [30]:

$$\frac{\partial \rho}{\partial t} + \frac{\partial}{\partial x_i}(\rho \overline{v}_i) = 0 \tag{7}$$

$$\frac{\partial}{\partial t}(\rho \overline{v}_i) + \frac{\partial}{\partial x_j}(\rho \overline{v}_i \overline{v}_j) = -\frac{\partial p}{\partial x_i} + \frac{\partial}{\partial x_j}[\mu(\frac{\partial \overline{v}_i}{\partial x_j} + \frac{\partial \overline{v}_j}{\partial x_i} - \frac{2}{3}\frac{\overline{v}_l}{x_l}\delta_{ij})] + \frac{\partial}{\partial x_j}(\rho \overline{v_i' v_j'}) + F_i \tag{8}$$

where $\rho$ is the density of the fluid, $v_i$ is the velocity component, $p$ is the total pressure, $F_i$ is the external body force component, and $\mu$ is the dynamic viscosity. The velocity $v_i$ is the sum of the time-averaged values $\overline{v}_i$ and the fluctuations $v_i'$.

### 3.2. Computational Domains and Grid Generation

Numerical simulations were used to assess the effect of the trough on the hydrodynamic properties of the HATTs, with the specific parameters shown in Table 1. The CFD model solves the RANS equation by a finite volume discretization scheme in the FLUENT environment. The turbulence term of the RANS equation is simulated by the SST k-ω turbulence model, which has been widely used in horizontal axis turbine studies [45] and has proven successful in simulating turbulence on airfoils [46]. It is known for its strong and dependable performance in forecasting various flow phenomena, such as free shear flow, boundary layer development, unfavorable pressure gradients, and boundary layer separation. Combining elements from both the k-ε and standard k-ω models, it offers accurate insights into the dynamics of boundary layers, particularly in situations involving transition, separation, and stall. The MRF is used to simulate the rotating motion of blades in the rotating sub-domain, which has been proved by Tran Ngoc Tu [47] to be a suitable method for simulating the characteristics of propellers in open water. Each domain can move at a different rotation/translation speed in the MRF simulation process. This method simulates the rotation/translation domain.

**Table 1.** Rotor parameters.

| | |
|---|---|
| Number of blade $B$ [–] | 3 |
| Rotor diameter $D$ [m] | 1.2 |
| Hub radius $R_h$ [m] | 0.12 |
| Rotor radius $R_b$ [m] | 0.6 |
| Local chord length $c$ [m] | 0.081~0.096 |
| Slot exit position $X$ [m] | 0.35$c$, 0.4$c$, 0.45$c$, 0.5$c$ |
| Slot exit width $t$ [m] | 0.03$c$, 0.04$c$, 0.05$c$, 0.06$c$, 0.07$c$ |
| Slot length $l$ [m] | 0.5$R_b$, 0.6$R_b$, 0.7$R_b$, 0.8$R_b$ |
| Free-stream velocity $V_0$ [m/s] | 0.5 |
| Turbulence intensity $T_i$ [%] | 3 |
| Sea water density $\rho$ [kg/m$^3$] | 1024 |
| Rotational speed $\omega$ [rad/s] | 1.67~6.67 |
| Tip-speed ratio $TSR$ [–] | 2~8 |

In consideration of the turbine's symmetrical nature, the computational domain consists of a solitary blade encompassing a one-third sector measuring 6D in diameter and 11D in length [48]. Positioned at a distance of 3D from the flow field inlet, the turbine is situated on the horizontal axis of symmetry. To enable the simulation of rotor rotation, the entire domain is divided into two subdomains, necessitating the application of boundary conditions at the interface where two subdomains interact. All computational subdomains are created using a hexahedral mesh, as depicted in Figure 2. The y+ value of the initial layer element on the blade surface is set in close proximity to 1.

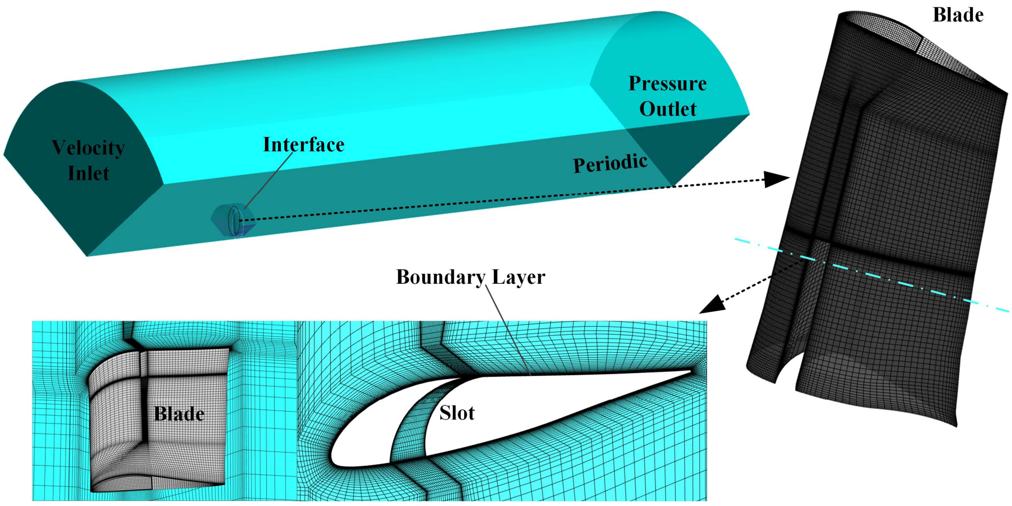


**Figure 2.** Computation domain and details of the mesh.

Specific boundary conditions are included, as follows:

(1) Inlet: Uniform steady velocity of 0.5 m/s.
(2) Outlet: Pressure outlet with a relative atmospheric pressure of 0 Pa.
(3) Interface: The boundary between the rotating and stationary domains is set as the interface boundary.
(4) Periodic boundary: The periodic boundary conditions for rotation are applied to the sidewall surfaces.
(5) No sliding wall: A no-sliding-wall condition is imposed on the blade surface.

### 3.3. Solution Settings

The steady-state MRF technique is employed to model the rotational movement of the rotor, utilizing a convergence criterion where the scaling residuals must be below $1 \times 10^{-6}$. In order to achieve rapid convergence, the SIMPLEC algorithm is employed as the pressure–velocity coupling method for all simulations. The pressure and momentum equations are discretized using the second-order upwind space discretization algorithm. The simulations were executed on a Dell T7810 workstation, equipped with 20 CPU cores and 64 GB of RAM. Each individual simulation required approximately 5 h to complete.

## 4. Results Discussion

### 4.1. Numerical Model Validation

In order to ascertain the grid independence of the numerical model, a total of four grid configurations with different node densities were employed to conduct a comparative analysis of the simulation outcomes. The outcomes are presented in Table 2. It is discernible that once the number of grids surpasses 3.5 million, the augmentation in grid density exhibits negligible influence on the calculated values of turbine power coefficients and thrust coefficients (with variations less than 3%). Therefore, we chose a moderately coarse mesh consisting of 3.5 million nodes to ensure that computational resources are conserved and that the mesh resolution in future simulations remains essentially the same as in the validation case described above.

**Table 2.** Grid independence verification results.

| Number of Grids | 2,300,000 | 3,500,000 | 5,000,000 | 6,200,000 |
|---|---|---|---|---|
| $C_P$ | 0.374 | 0.385 | 0.391 | 0.393 |
| $C_T$ | 0.644 | 0.664 | 0.673 | 0.676 |

To assess the acceptability of the numerical model, a comparison was made between the turbine torques obtained from simulations and those measured experimentally. The experiment was carried out in a towing tank of the Key Laboratory of the Ministry of Industry and Information Technology of Northwestern Polytechnical University. The towing tank is shown in Figure 3, and has a total length of 180 m, a water depth of 6 m, a width of 7 m, and a maximum test speed of 7 m/s. The turbine torque test device was mounted on the interface of the trailer. During the experiment, the submergence depth of the hydraulic turbine was kept at 1 m, and the towing speed was 0.5 m/s. The blockage ratio of the turbine during the towing tank was 2.7%, which is the ratio of the swept area of the turbine to the cross-sectional area of the towing tank.

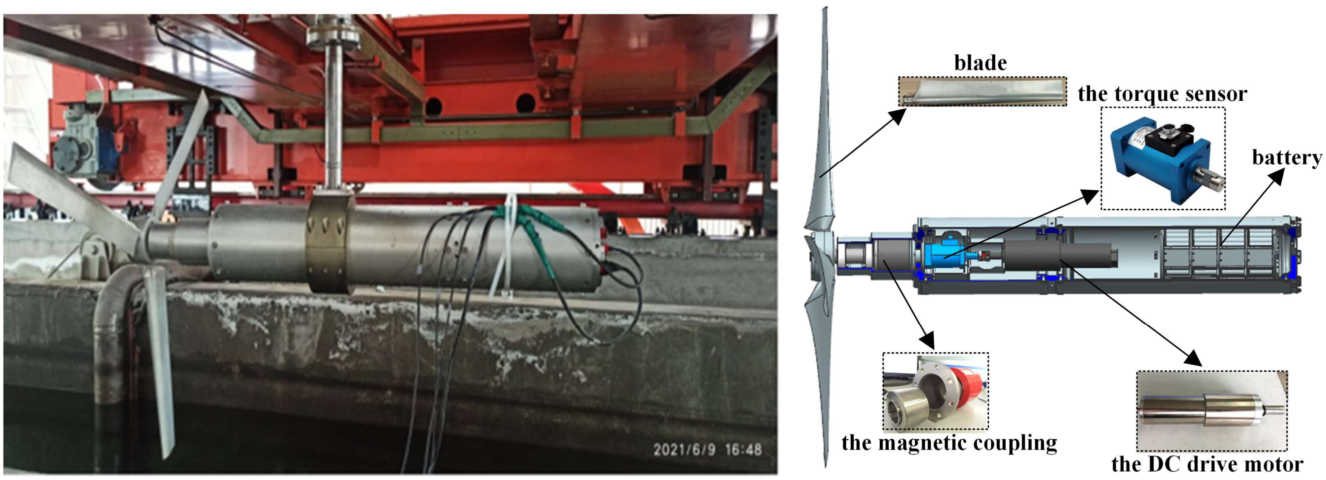


**Figure 3.** Turbine torque test device and installation schematic.

To test the torque characteristics of the turbine, the turbine torque test device was designed, as shown in Figure 3. The device is mainly composed of the turbine, the magnetic coupling, a torque sensor, a DC drive motor, and a sealed casing. Among these, the magnetic coupler is composed of an isolation cover and magnetic poles on both sides of the isolation cover, and its function is to transfer the driving torque of the DC motor to the turbine through magnetic force. The DC drive motor is the component that drives the turbine, and a Maxon RE 65 motor with a rated power of 250 W was chosen. The GP 81A planetary gear reducer with a reduction ratio of 93:1 was used in conjunction with the DC motor. The torque sensor is one of the most important components of the turbine torque test device, and can measure the torque on the blades when the turbine is running at a certain tip-speed ratio. A DY-200 dynamic torque sensor with a measuring range of 0~50 N·m and measuring accuracy of 0.1% was used in this research. The working process of the turbine torque test device is as follows: the driving function of the DC motor transmits the torque to the turbine through the magnetic coupling so that the turbine rotates at a certain speed, and the speed of the motor can be changed by changing the voltage of the motor. At the same time, the test device follows the trailer at a constant speed of 0.5 m/s, and the torque received by the turbine in a uniform flow is captured by the dynamic torque sensor. The entire test process was completed in June 2021. The data were obtained through the host computer to collect the test data in the DY-200 dynamic torque sensor. The specific testing and commissioning process is illustrated in Figure 4.

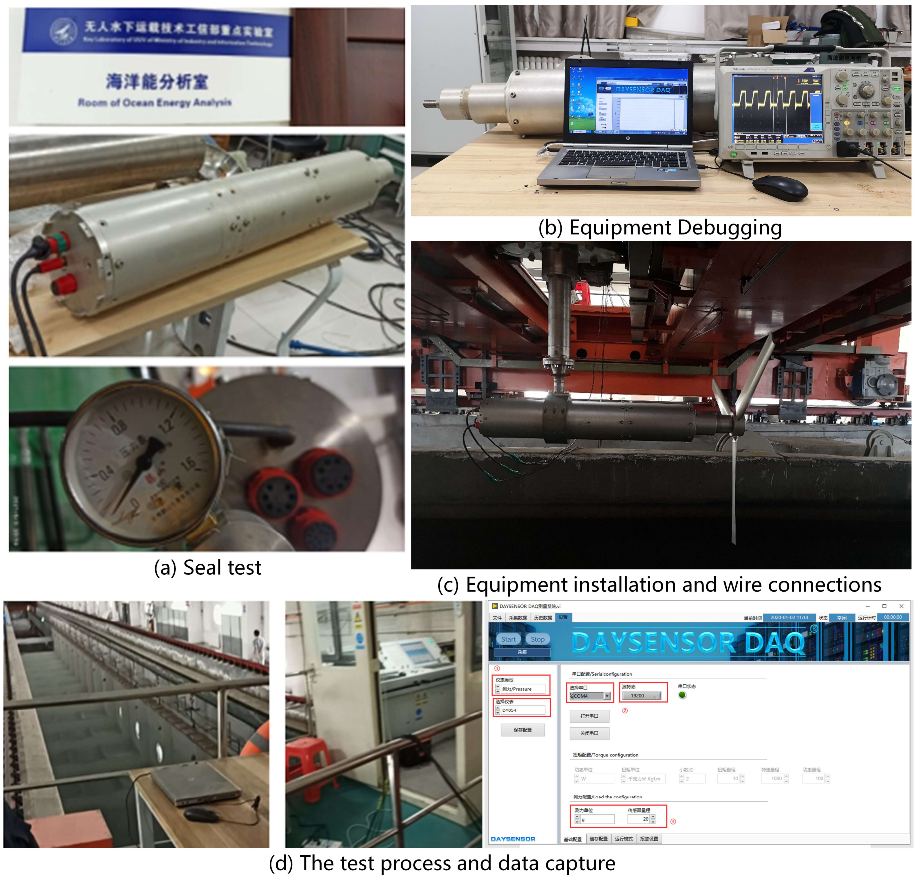


**Figure 4.** The installation and debugging of test equipment.

The turbine torque as monitored by the dynamic torque sensor when the $TSR = 6$ is shown in Figure 5a; this sensor collects 80 data points per second. The fluctuation of the torque within a certain range is observed due to factors such as sensor sensitivity and device installation. Nevertheless, it can be inferred that the torque monitored by the sensor remains relatively stable.

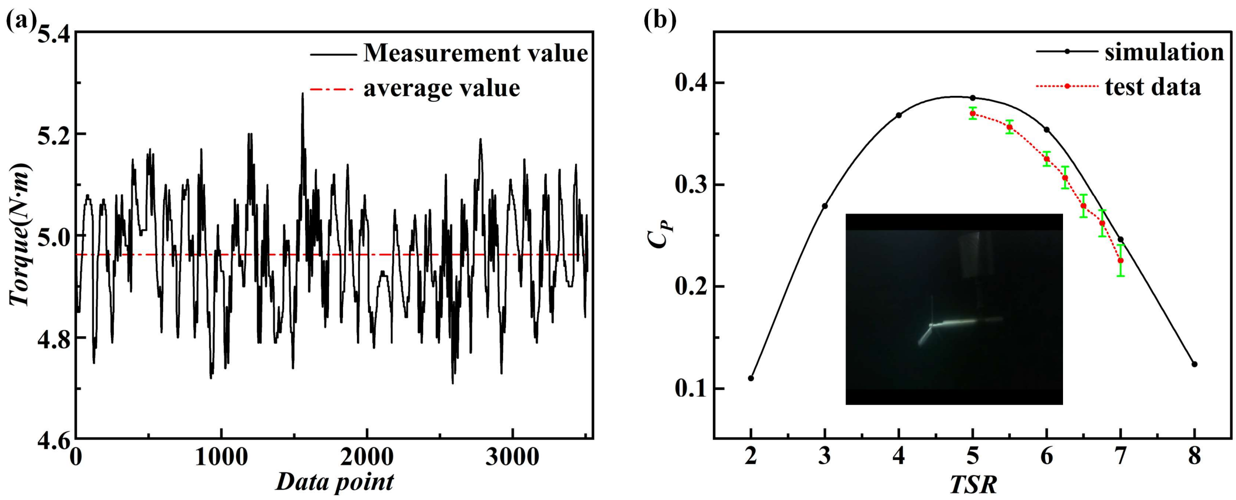


**Figure 5.** Results of tests and simulations: (**a**) monitoring value, (**b**) comparison of test and simulation results.

The experimental test results for the power coefficient factor are compared with the simulation value, and the findings are illustrated in Figure 5b. It is evident from the figure that the trend of the turbine power coefficient aligns with the simulation, with all errors being less than 10%. The discrepancy between CFD simulations and experimental methods can be attributed to the limited scope of CFD simulations, which solely focus on evaluating the efficiency of the rotor. However, these simulations fail to account for the energy losses that occur in the bearings and transmission processes. Thus, it can be concluded that the numerical model employed in this study is acceptable.

### *4.2. Hydrodynamic Characteristics of 2-D Slotted Hydrofoils*

Firstly, the flow control mechanism of the slotted hydrofoils was explained by the 2-D hydrofoil simulation results. In this study, the fx-77-w121 with a chord length of 100 mm was selected as the reference hydrofoil, and the uniform incoming flow was set to 2 m/s. The effect of slots on hydrofoil performance was studied at a Reynolds number of $2 \times 10^5$.

The positioning of the slot on a hydrofoil plays a crucial role in determining where the injection of fluid kinetic energy occurs on the suction surface. This, in turn, has a notable impact on the hydrodynamics of the hydrofoil. In this particular study, the hydrodynamic characteristics of slotted hydrofoils with varying exit positions and a fixed exit width ($t = 0.04c$) were thoroughly examined. The findings, as depicted in Figure 6, reveal that the presence of slots does not always lead to enhanced hydrofoil performance. When the angle of attack is below 12°, the hydrodynamic behavior of the slotted hydrofoil is inferior to that of the clear hydrofoil. However, when the angle of attack surpasses 12°, it demonstrates superior performance. Specifically, the lift coefficient of the hydrofoil can increase by up to 43% at an angle of attack of 16°, while the maximum increase in the lift-to-drag ratio is 166%, achieved at an angle of attack of 14°. Furthermore, it is worth noting that the presence of the slot significantly delays the stall angle of the hydrofoil, pushing it from 10° to approximately 16°. Notably, the closer the exit position of the slot to the leading edge, the more pronounced the slot's effect in improving the hydrofoil's lift and lift-to-drag ratio becomes.

The investigation focused on the impact of varying exit widths of slots on hydrofoil performance, as the magnitude of fluid momentum injected into the pressure surface of the hydrofoil is determined by the exit width of the slot. Figure 7 presents the lift–drag curves of slotted hydrofoils with exit widths ranging from $0.03c$ to $0.07c$, while maintaining a fixed exit position at $X = 0.4c$. It can be observed that the lift and drag curves of all slotted hydrofoils exhibit similarity. Furthermore, an increase in slot exit width corresponds to an increase in lift coefficient and a decrease in drag coefficient.

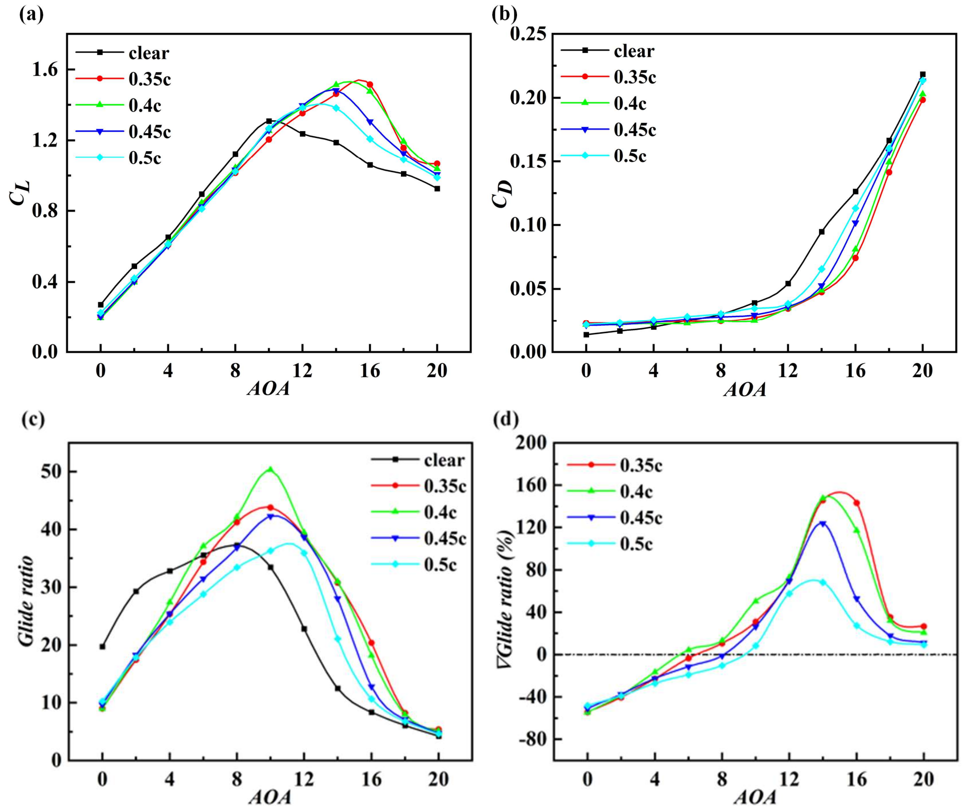


**Figure 6.** The influence of slot exit position on the hydrodynamics of hydrofoils: (**a**) lift coefficient, (**b**) drag coefficient, (**c**) lift-to-drag ratio, (**d**) relative increment in glide ratio (%).

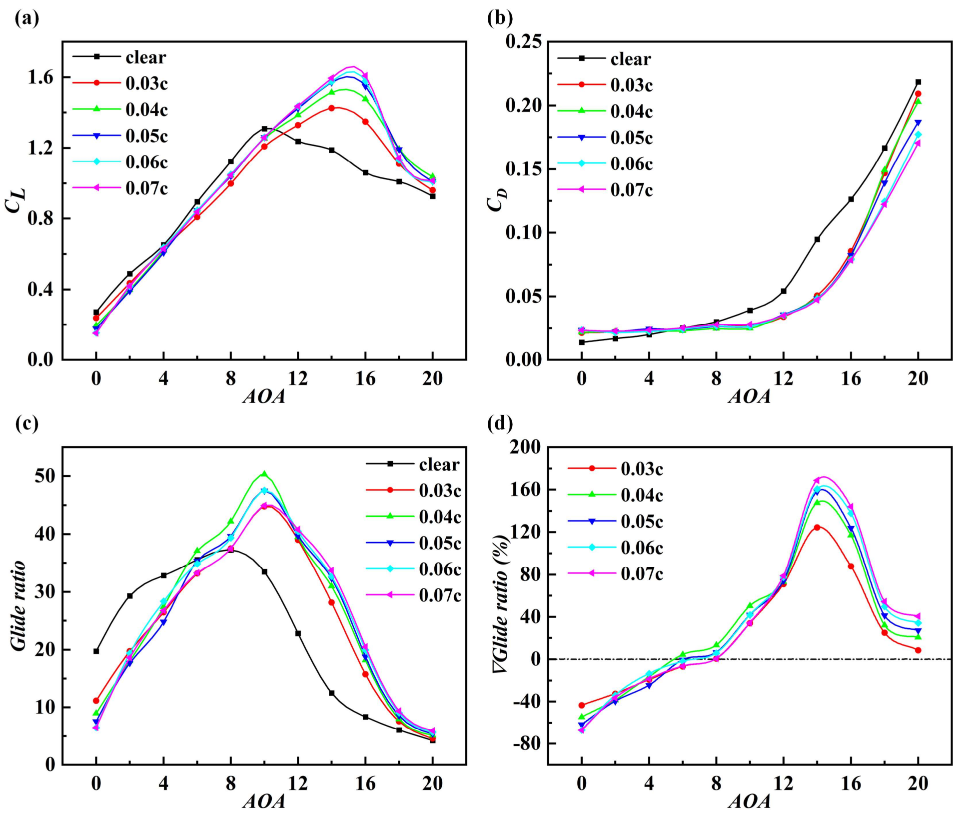


**Figure 7.** The influence of slot exit width on the hydrodynamics of hydrofoils: (**a**) lift coefficient, (**b**) drag coefficient, (**c**) lift-to-drag ratio, (**d**) relative increment in glide ratio (%).

*4.3. Analysis of the Passive Fluid Control Mechanism of the Slot*

In order to examine the mechanism by which the slot affects hydrofoil performance, the velocity contours of the flow field were analyzed for both a clean hydrofoil and a slotted hydrofoil before and after stall, as depicted in Figure 8a. From the figure, it is evident that the hydrofoil surface experiences laminar flow at low angles of attack, and the presence of the slot on the hydrofoil leads to a slight reduction in velocity on its upper surface. The clean hydrofoil exhibits flow separation at an angle of attack of 16°, whereas the slot significantly inhibits flow separation, thereby improving the flow field characteristics of the hydrofoil. Furthermore, the velocity of the leading edge of the slotted hydrofoil is substantially higher compared to that of the clean hydrofoil. Figure 8b portrays the relationship between the slot exit width, the growth rate of the lift-to-drag ratio, and the slot exit volume flow rate. Within a specific range, there is a linear and positive correlation between the volume flow rate of the slot and its width. Additionally, the changing trend of the lift–drag growth rate aligns closely with the changing trend of the volume flow rate.

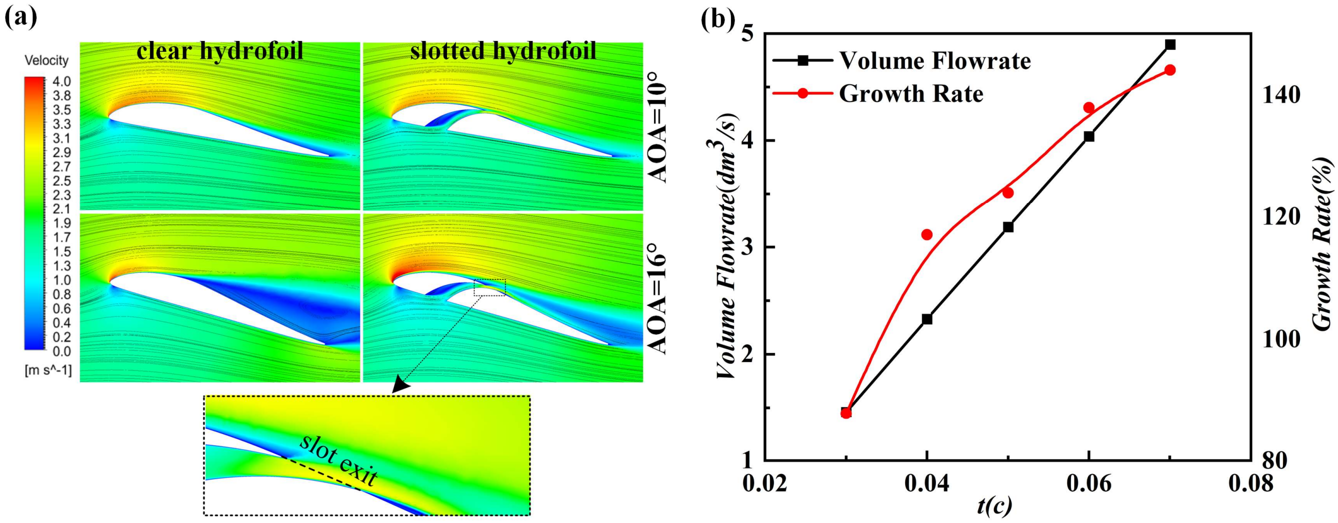


**Figure 8.** The effect of a slot on the hydrofoil flow field (velocity distribution): (**a**) velocity contours; (**b**) growth rate of lift-to-drag ratio and slot exit volume flow rate.

Figure 9a,b exhibit the flow field pressure contours and pressure distribution diagrams for clean and slotted hydrofoils at angles of attack of 10° and 16°, respectively. Upon comparing the pressure contours of the two hydrofoils at an angle of attack of 10°, it becomes apparent that the pressure disparity between the upper and lower surfaces of the slotted hydrofoil decreases as a result of its specific geometric configuration. This decrease in pressure differential accounts for the decline in the lift coefficient of the slotted hydrofoil. Conversely, when the angle of attack is increased to 16°, the slot significantly amplifies the area of negative pressure on the upper surface of the hydrofoil. Consequently, the pressure difference between the upper and lower surfaces of the hydrofoil experiences a substantial increase. This observation confirms the assertion that the lift coefficient of a slotted hydrofoil is enhanced at high angles of attack.

A fluid in motion possesses inherent kinetic energy, which acts as a deterrent against unfavorable pressure gradients. However, in cases where the inflow velocity and kinetic energy are relatively low, the opposing adverse pressure gradient becomes dominant, leading to the occurrence of flow separation. The post-stall flow fields for a clean hydrofoil and slotted hydrofoils of varying configurations were compared, with the results depicted in Figure 10. The hydrofoil flow field is significantly influenced by the geometric parameters of the slot. As the slot's exit position approaches the transition point, it becomes more effective at preventing flow separation of the hydrofoil. An example of this is seen when the exit position is at 0.35$c$, where the slotted hydrofoils exhibit obvious suppression of flow separation compared to clear hydrofoils. Furthermore, a wider slot exit width enhances the suppression effect on hydrofoil flow separation. This is due to the increased injection of fluid momentum from the hydrofoil pressure surface into the hydrofoil suction surface, which becomes more significant as the slot exit width increases.

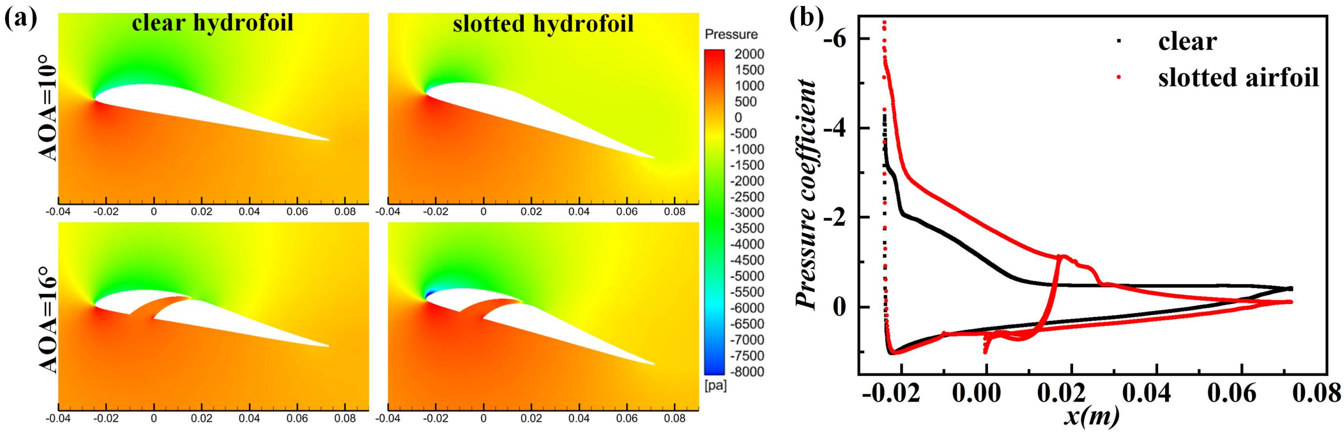


**Figure 9.** The effect of a slot on the hydrofoil flow field (pressure distribution): (**a**) pressure contours, (**b**) pressure distribution on the hydrofoil.

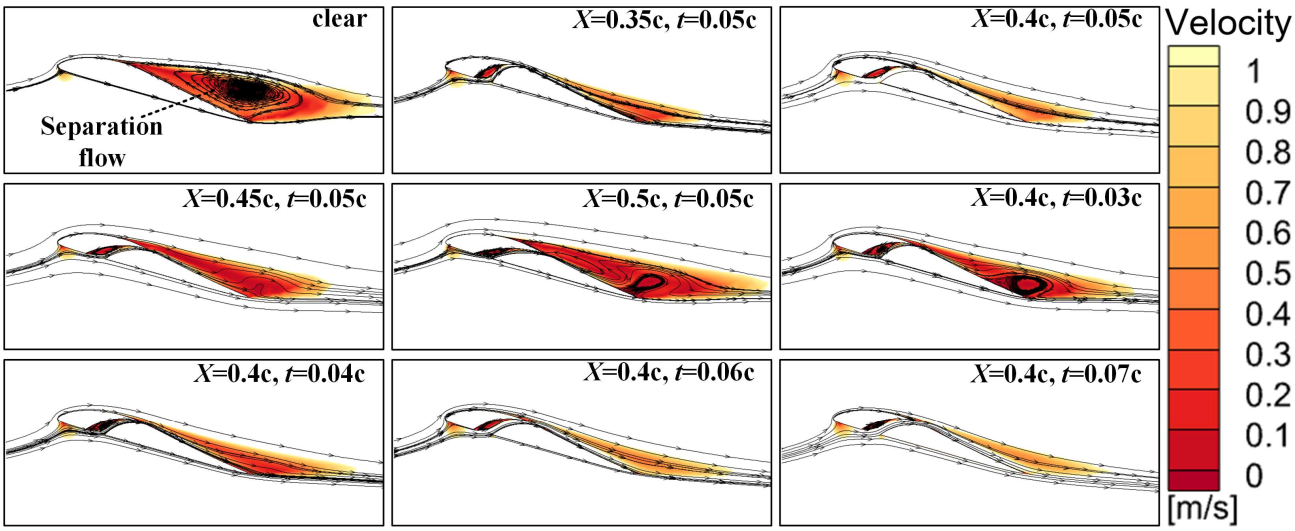


**Figure 10.** Separation flow of different slotted hydrofoils.

*4.4. Hydrodynamic Characteristics of the Three-Dimensional Slotted Blade*

To analyze the impact of the slot geometry configuration on turbine blade performance, three simulation results are discussed, including the effect of slot exit width, slot exit location, and slot span length on blade performance.

The hydrodynamic characteristics of the 2-D hydrofoil are significantly impacted by position of the slot exit, as indicated by the simulation results. Hence, the width of the slots is fixed at $0.05c$, and the span length is fixed at $0.5R$, calculating the power coefficients of the blade at different slot exit positions ($0.35c$–$0.5c$). The results displayed in Figure 11 demonstrate that the slot enhances the hydrodynamic performance of the blade at low tip-speed ratios. Furthermore, the lifting effect is improved when the slot exit is closer to the transition point. When the exit position is at 0.4c and $TSR = 3$, the slot increases the power coefficient by 5%. It should be noted that the presence of the slot influences the optimal tip-speed ratio. While the clear blade attains its maximum value at $TSR = 5$, the slotted blade exhibits optimal performance at approximately $TSR = 4$.

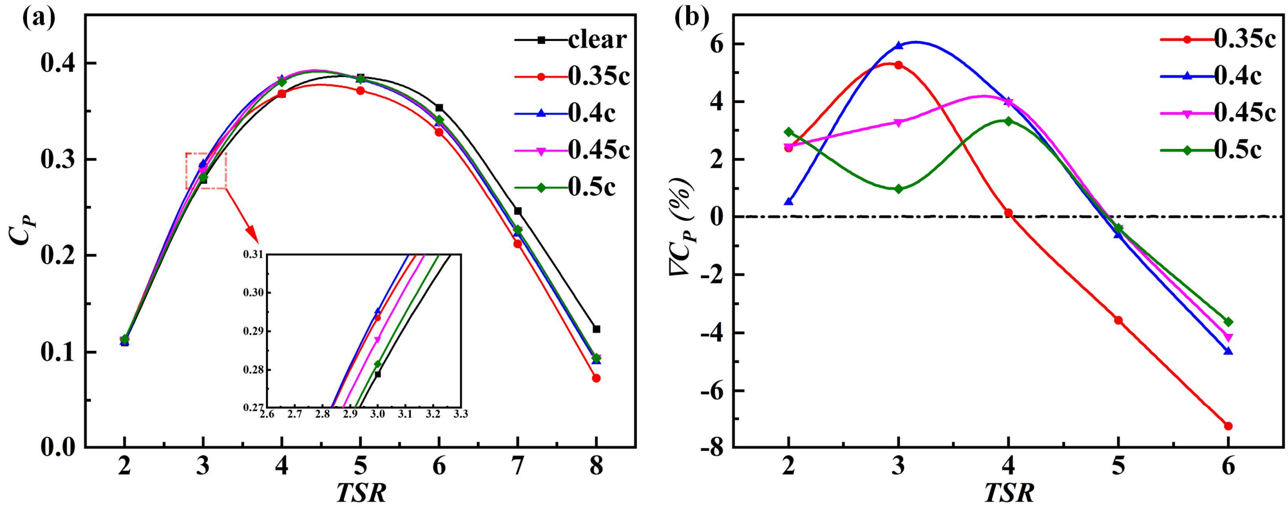


**Figure 11.** Variation in blade performance with slot exit position: (**a**) power coefficient, (**b**) relative increment in *Cp* (%).

To examine the impact of the slot on the velocity flow field, a study was conducted wherein the velocity distribution of the blade was observed on various cross-sections, as depicted in Figure 12. At a *TSR* of 3, significant flow separation was observed at both the blade root (0.3*R*) and the middle region (0.5*R*). Conversely, the presence of slots on the blades exhibited the ability to mitigate flow separation to some extent. The injection of a high-momentum jet through the slot onto the suction surface effectively suppressed or weakened flow separation when the slot was positioned upstream of the separation region. Alternatively, when the slot was placed within the separation region, the separated flow was divided into multiple regions by the jet, leading to a reduction in flow separation in these areas. As a result, the slotted blades demonstrated exceptional hydrodynamic performance.

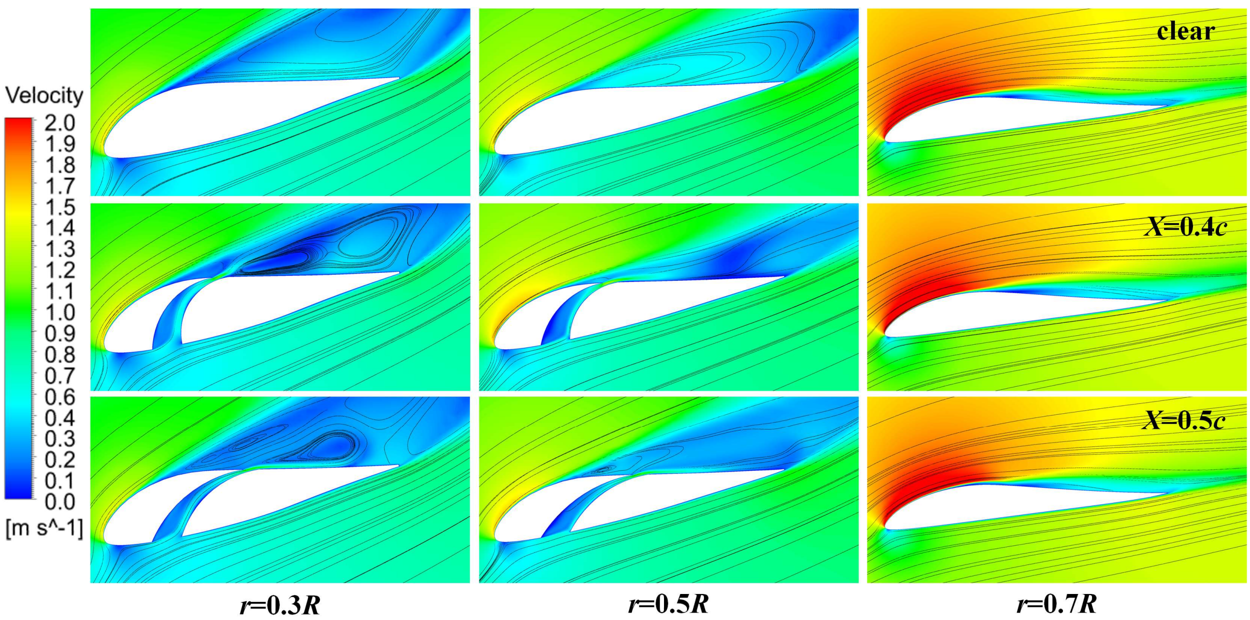


**Figure 12.** Velocity contours of different slotted blades (*TSR* = 3).

The investigation conducted in this study focused on evaluating the hydrodynamic performance of slotted blades with varying exit widths, as illustrated in Figure 13. The position of the slots' exit remains fixed at a value of 0.4*c*, while the spanwise length is consistently maintained at 0.5*R*. The results indicate that, at lower tip-speed ratios, the inclusion of a slot leads to an enhancement in the power coefficient of the blades. Moreover, this increase in power coefficient becomes more pronounced with larger exit widths. Notably, when the exit width is set to 0.07*c* and the tip-speed ratio is 3, the power coefficient of the slotted blade exhibits the most significant rise, amounting to 7.8%. Conversely, at higher tip-speed ratios, the power coefficient experiences a reduction due to the presence of the slot, with the magnitude of this decrease being directly proportional to the exit width. At a tip-speed ratio of 7, the power coefficient of the slotted blade undergoes a maximum decline of 12%.

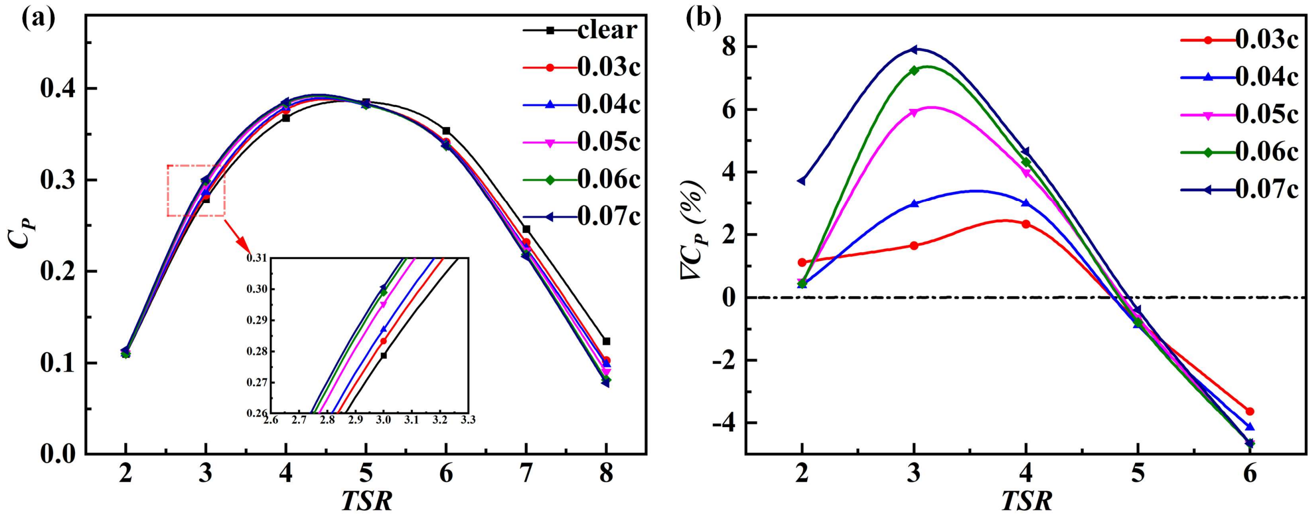


**Figure 13.** Variation in blade performance with slot exit width: (**a**) power coefficient, (**b**) relative increment in *Cp* (%).

The consequences of the dynamic flow characteristics caused by the slots were examined in greater detail through the visualization of reverse flow patterns surrounding the blades. In this study, the flow behavior of a blade with slot exit widths of 0.05*c* and 0.07*c* was investigated at a *TSR* of 3. As depicted in Figure 14, the flow distribution along the span of the blade following a stall is presented. It is evident that the presence of slots can significantly enhance the mitigation of flow separation, particularly at low tip-speed ratios. Furthermore, it is noteworthy that the wider the slot exit, the more pronounced the inhibitory effect on blade flow separation becomes.

The radial flow of an ocean current turbine blade is a significant factor that cannot be disregarded. Hence, the impact of the span length of the slot on the blade should also be taken into consideration. In order to examine the effect of the slot on the hydrodynamics of the blade, the span length of the slots was altered and the outcomes are presented in Figure 15. It is evident that the span length of the slot has a notable influence on the power coefficient. Specifically, a larger span length results in a more pronounced improvement in the blade power coefficient at low tip-speed ratios, while also leading to a greater decrease in the blade power coefficient at high tip-speed ratios.

The pressure distribution and flow separation on the suction surface of the blade are depicted in Figure 16. When the tip-speed ratio is 3, the clear blade experiences complete separation on its suction surface, resulting in deep stall. The separation point occurs at approximately 20% of the chord length. The non-constant streamlines begin at the root of the blade due to the high local angle of attack, and then sweep radially outward towards the tip, as illustrated in Figure 16a. In contrast, the slotted blade delays the separation point due to the jet generated by the slots along the blade span. At a slot span of 0.8 R, the flow separation in the middle of the blade is considerably suppressed, and the streamlines remain attached. Moving on to a tip-speed ratio of 5, the clear blade exhibits partial flow separation on its surface. The separation region is observed at the root of the blade, with the separation point occurring at around 30% of the chord length, as shown in Figure 15b.

Similarly, slotted blades also experience flow separation, but the separation zone is confined to the chord length at the back end of the blade root, specifically at around 80% of the chord length. Furthermore, at lower tip-speed ratios, the presence of the slot causes an increase in negative pressure on the suction side of the blade, resulting in an enlargement of the negative pressure region and an increase in the pressure difference between the suction and pressure sides of the blade. In conclusion, the surface flow lines align with the analysis of the separation flow presented earlier.

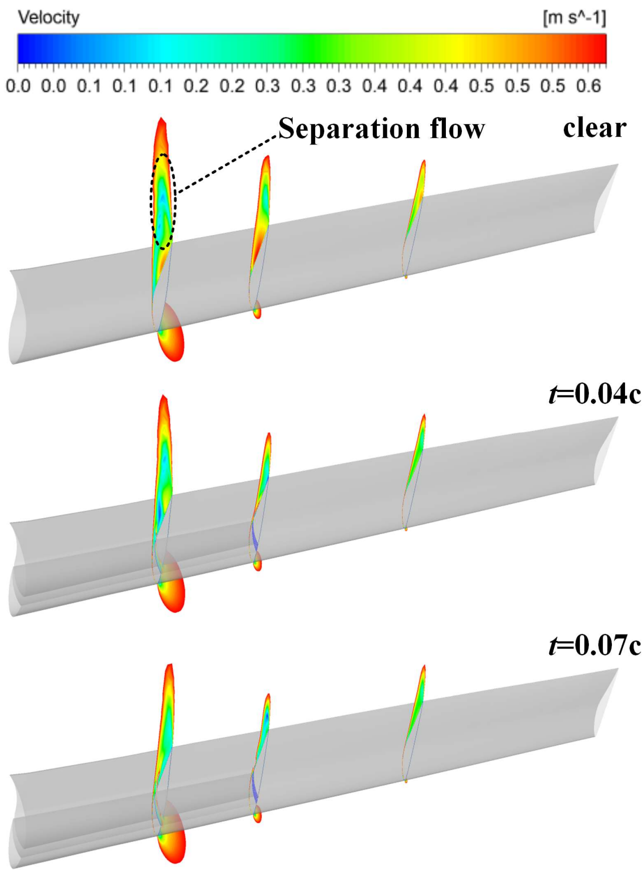


**Figure 14.** The effect of slots on blade separation flow (*TSR* = 3).

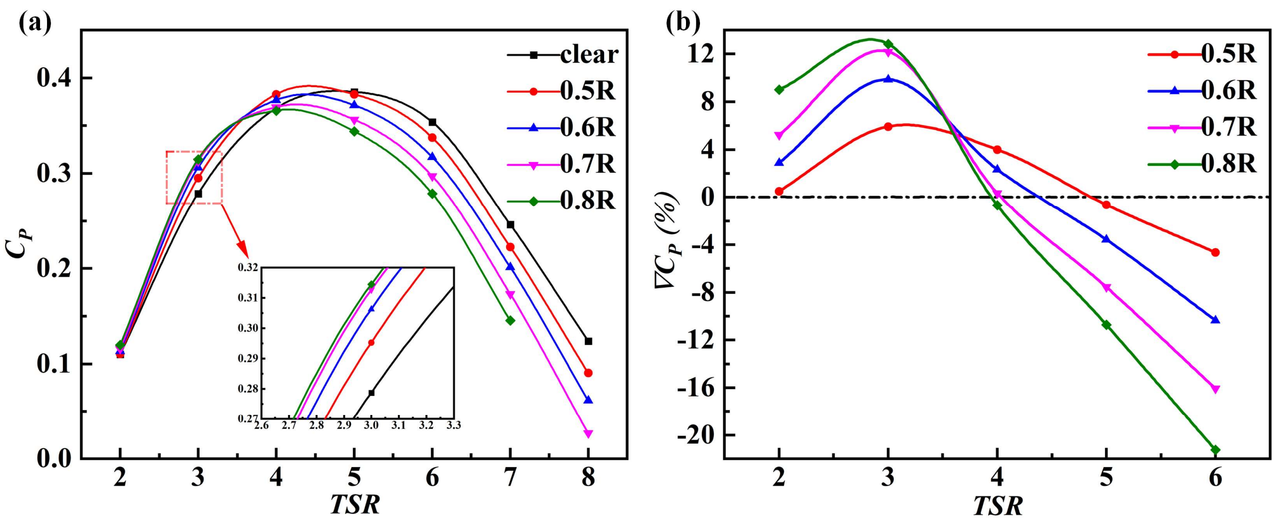


**Figure 15.** Variation in blade performance with slot length: (**a**) power coefficient, (**b**) relative increment in *Cp* (%).

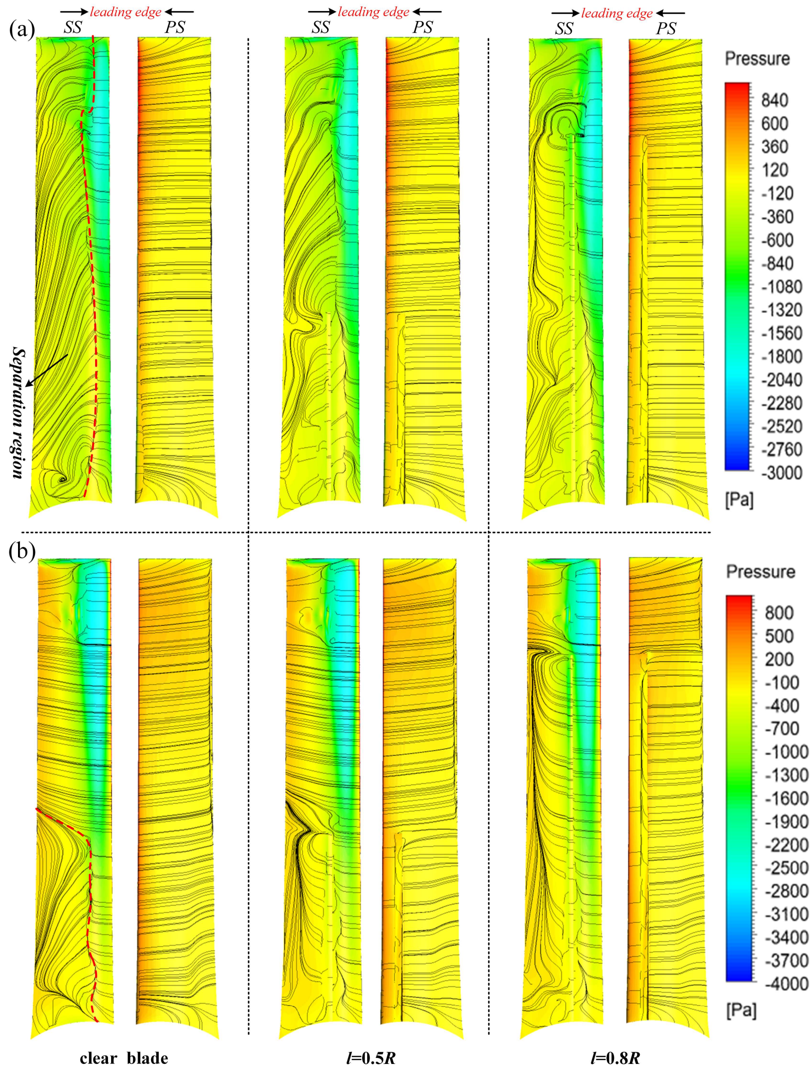


**Figure 16.** Pressure distribution on the blade with surface flow streamlines. (**a**) $TSR = 3$, (**b**) $TSR = 5$ ($SS$: suction surface; $PS$: pressure surface).

## 5. Conclusions

This research establishes the importance of slotted blade design for improving the performance of tidal turbines. Additionally, this study delves into the flow control mechanism of these slots, evaluates the relationship between the geometric parameters of the slots and the effectiveness of flow control, and ultimately determines the optimal configuration for the slotted blades. The discoveries made in this investigation hold great importance for enhancing the efficiency of power generation in tidal energy turbines. Moreover, this study contributes to the advancement and widespread implementation of slots as a passive flow control method in turbines. The conclusions can be summarized as follows: At low tip-speed ratios (large angles of attack), the slots can significantly improve the hydrodynamic performance of the blade, and the closer the exit of the slot to the transition point, the greater the width of the exit, and the greater the length of the slot in the span direction, the more pronounced the improvement in the blade performance. After applying the slot, the lift–drag ratio of two-dimensional hydrofoils is increased by a maximum of 166%, and the power coefficient of three-dimensional blades is increased by a maximum of 7.8%. Overall, the application of a slot can improve the power generation efficiency of ocean current turbines to a certain extent. In addition, a detailed hydrodynamic analysis revealed that the slot was shown to be effective in suppressing flow transitions and separation. It also revealed the relationship between fluid momentum and the slot exit.

The findings presented in this paper shed light on the effectiveness of employing flow control of slots for tidal energy turbines operating at low tip-speed ratios. However, it is important to note that this approach exhibits limitations in terms of its effectiveness and practicality. To enhance the range of the effectiveness of this mechanism, further investigation and experimentation on novel slot designs are imperative.

**Author Contributions:** Conceptualization, Z.M.; Data curation, G.Y.; Methodology, W.T.; Validation, T.Z.; Writing—original draft, G.Y.; Writing—review and editing, W.T. All authors have read and agreed to the published version of the manuscript.

**Funding:** This research was supported by the National Natural Science Foundation of China (Program No. 51809214).

**Institutional Review Board Statement:** Not applicable.

**Informed Consent Statement:** Not applicable.

**Data Availability Statement:** Not applicable.

**Conflicts of Interest:** The authors declare that they have no known competing financial interests or personal relationships that could have appeared to influence the work reported in this paper.

## Nomenclature

| | |
|---|---|
| $B$ | Number of blades [–] |
| $c$ | Local chord length [m] |
| $C_D$ | Drag coefficient [–] |
| $C_L$ | Lift coefficient [–] |
| $C_P$ | Power coefficient [–] |
| $Cpressure$ | Pressure coefficient [–] |
| $C_T$ | Thrust coefficient [–] |
| $D$ | Rotor diameter [m] |
| $l$ | Slot length [m] |
| $L$ | Lift force on the hydrofoil [N] |
| $M$ | Turbine torque [N·m] |
| $p$ | Pressure [Pa] |
| $p_\infty$ | The far-field pressure [Pa] |
| $r$ | Local radius [m] |
| $R_h$ | Hub radius [m] |
| $R_b$ | Rotor radius [m] |
| $S$ | Area of the hydrofoil [m$^2$] |
| $t$ | Slot exit width [m] |
| $T$ | Turbine thrust [N] |
| $T_i$ | Turbulence intensity [%] |
| $V_0$ | Free-stream velocity [m/s] |
| $X$ | Slot exit position [m] |
| $\rho$ | Sea water density [kg/m$^3$] |
| $\omega$ | Rotor rotation speed [rad/s] |
| 2-D | two-dimensional |
| 3-D | three-dimensional |
| AOA | angle of attack |
| CFD | computational fluid dynamics |
| HATT | horizontal axis tidal turbine |
| MRF | multi-reference frame |
| RANS | Reynolds Averaged Navier–Stokes |
| SST | shear stress transport |
| TSR | tip-speed ratio |

## References


1. Melikoglu, M. Vision 2023: Status quo and future of biomass and coal for sustainable energy generation in Turkey. *Renew. Sustain. Energy Rev.* **2017**, *74*, 800–808. [CrossRef]
2. Melikoglu, M. Shale gas: Analysis of its role in the global energy market. *Renew. Sustain. Energy Rev.* **2014**, *37*, 460–468. [CrossRef]
3. El-Farra, N.H.; Christofides, P.D. Special issue on "control and optimization of renewable energy systems". *Renew. Energy* **2017**, *100*, 1–2. [CrossRef]
4. Gul, M.; Tai, N.; Huang, W.; Nadeem, M.H.; Yu, M. Assessment of Wind Power Potential and Economic Analysis at Hyderabad in Pakistan: Powering to Local Communities Using Wind Power. *Sustainability* **2019**, *11*, 1391. [CrossRef]
5. Zhang, J.S.; Gao, P.; Zheng, J.H.; Wu, X.G.; Peng, Y.X.; Zhang, T.T. Current-induced seabed scour around a pile-supported horizontal-axis tidal stream turbine. *J. Mar. Sci. Technol.* **2015**, *23*, 929–936. [CrossRef]
6. Abuan, B.E.; Howell, R.J. The performance and hydrodynamics in unsteady flow of a horizontal axis tidal turbine. *Renew. Energy* **2019**, *133*, 1338–1351. [CrossRef]
7. Soleimani, K.; Ketabdari, M.J.; Khorasani, F. Feasibility study on tidal and wave energy conversion in Iranian seas. *Sustain. Energy Technol. Assess.* **2015**, *11*, 77–86. [CrossRef]
8. Hassan, H.F.; El-Shafie, A.; Karim, O.A. Tidal current turbines glance at the past and look into future prospects in Malaysia. *Renew. Sustain. Energy Rev.* **2012**, *16*, 5707–5717. [CrossRef]
9. Xu, Q.; Li, W.; Lin, Y.; Liu, H.; Gu, Y. Investigation of the performance of a stand-alone horizontal axis tidal current turbine based on in situ experiment. *Ocean Eng.* **2016**, *113*, 111–120. [CrossRef]
10. Andritz Hydro Hammerfest. Renewable Energy from Tidal Currents. 2015. Available online: https://orbitalmarine.com/O2 (accessed on 13 March 2023).
11. Atlantis Resources. Ar1500 Tidal Turbine. 2016. Available online: https://simecatlantis.com/wp-content/uploads/2016/08/AR1500-Brochure-Final-1.pdf (accessed on 10 March 2023).
12. Orbital Marine Power. Orbital o2 2mw. 2021. Available online: https://orbitalmarine.com/O2 (accessed on 10 March 2023).
13. Sazonov, Y.A.; Mokhov, M.A.; Gryaznova, I.V.; Voronova, V.V.; Tumanyan, K.A.; Frankov, M.A.; Balaka, N.N. Computational Fluid Dynamics (CFD) Simulation of Mesh Jet Devices for Promising Energy-Saving Technologies. *Civ. Eng. J.* **2022**, *8*, 2749–2767. [CrossRef]
14. Sazonov, Y.A.; Mokhov, M.A.; Gryaznova, I.V.; Voronova, V.V.; Tumanyan, K.A.; Frankov, M.A.; Balaka, N.N. Designing Mesh Turbomachinery with the Development of Euler's Ideas and Investigating Flow Distribution Characteristics. *Civ. Eng. J.* **2022**, *8*, 2598–2627. [CrossRef]
15. Tiainen, J.; Grönman, A.; Jaatinen-Värri, A.; Backman, J. Flow Control Methods and Their Applicability in Low-Reynolds-Number Centrifugal Compressors—A Review. *Int. J. Turbomach. Propuls. Power* **2018**, *3*, 2. [CrossRef]
16. Yavuz, T.; Koç, E.; Kaynak, B. Hydrodynamics performance of hydrofoil-slat arrangements in 3D analysis. *Energy Convers. Manag.* **2013**, *75*, 44–50. [CrossRef]
17. Wei, Q.; Chen, H.-X.; Zhang, R. Numerical research on the performances of slot hydrofoil. *J. Hydrodyn.* **2015**, *27*, 105–111. [CrossRef]
18. Liu, C.; Yan, Q.; Wood, H.G. Numerical investigation of passive cavitation control using a slot on a three-dimensional hydrofoil. *Int. J. Numer. Methods Heat Fluid Flow* **2019**, *30*, 3585–3605. [CrossRef]
19. Belamadi, R.; Djemili, A.; Ilinca, A.; Mdouki, R. Aerodynamic performance analysis of slotted airfoils for application to wind turbine blades. *J. Wind. Eng. Ind. Aerodyn.* **2016**, *151*, 79–99. [CrossRef]
20. Moshfeghi, M.; Nur, N. Numerical investigation on the coanda effect over the s809 airfoil with synthetic jet actuator at high angle of attack. In Proceedings of the 4th ASME Joint US-European Fluids Engineering Division Summer Meeting, Chicago, IL, USA, 3–7 August 2014.
21. Xie, Y.; Chen, J.; Qu, H.; Xie, G.; Zhang, D.; Moshfeghi, M. Numerical and Experimental Investigation on the Flow Separation Control of S809 Airfoil with Slot. *Math. Probl. Eng.* **2013**, *2013*, 301748. [CrossRef]
22. Beyhaghi, S.; Amano, R.S. Improvement of Aerodynamic Performance of Cambered Airfoils Using Leading-Edge Slots. *J. Energy Resour. Technol.* **2017**, *139*, 051204. [CrossRef]
23. Kundu, P. Hydrodynamic performance improvement on small horizontal axis current turbine blade using different tube slots configurations. *Appl. Ocean Res.* **2019**, *91*, 101873. [CrossRef]
24. Ni, Z.; Dhanak, M.; Su, T.-C. Improved performance of a slotted blade using a novel slot design. *J. Wind. Eng. Ind. Aerodyn.* **2019**, *189*, 34–44. [CrossRef]
25. Ni, Z.; Dhanak, M.; Su, T.-C. Performance of a slotted hydrofoil operating close to a free surface over a range of angles of attack. *Ocean Eng.* **2019**, *188*, 106296. [CrossRef]
26. Mohamed, O.S.; Ibrahim, A.A.; Etman, A.K.; Abdelfatah, A.A.; Elbaz, A.M. Numerical investigation of Darrieus wind turbine with slotted airfoil blades. *Energy Convers. Manag. X* **2020**, *5*, 100026. [CrossRef]
27. Abdolahifar, A.; Karimian, S. A comprehensive three-dimensional study on Darrieus vertical axis wind turbine with slotted blade to reduce flow separation. *Energy* **2022**, *248*, 123632. [CrossRef]
28. Tian, W.; VanZwieten, J.H.; Pyakurel, P.; Li, Y. Influences of yaw angle and turbulence intensity on the performance of a 20 kW in-stream hydrokinetic turbine. *Energy* **2016**, *111*, 104–116. [CrossRef]

29. Tian, L.; Song, Y.; Zhao, N.; Shen, W.; Zhu, C.; Wang, T. Effects of turbulence modelling in AD/RANS simulations of single wind & tidal turbine wakes and double wake interactions. *Energy* **2020**, *208*, 118440. [CrossRef]
30. Bahaj, A.S.; Molland, A.F.; Chaplin, J.R.; Batten, W.M.J. Power and thrust measurements of marine current turbines under various hydrodynamic flow conditions in a cavitation tunnel and a towing tank. *Renew. Energy* **2007**, *32*, 407–426. [CrossRef]
31. Kolekar, N.; Banerjee, A. Performance characterization and placement of a marine hydrokinetic turbine in a tidal channel under boundary proximity and blockage effects. *Appl. Energy* **2015**, *148*, 121–133. [CrossRef]
32. Badshah, M.; VanZwieten, J.; Badshah, S.; Jan, S. CFD study of blockage ratio and boundary proximity effects on the performance of a tidal turbine. *IET Renew. Power Gener.* **2019**, *13*, 744–749. [CrossRef]
33. Amiri, H.A.; Shafaghat, R.; Alamian, R.; Taheri, S.M.; Shadloo, M.S. Study of horizontal axis tidal turbine performance and investigation on the optimum fixed pitch angle using CFD A case study of Iran. *Int. J. Numer. Methods Heat Fluid Flow* **2020**, *30*, 206–227. [CrossRef]
34. Lee, N.J.; Kim, I.C.; Kim, C.G.; Hyun, B.S.; Lee, Y.H. Performance study on a counter-rotating tidal current turbine by CFD and model experimentation. *Renew. Energy* **2015**, *79*, 122–126. [CrossRef]
35. Liu, J.; Lin, H.; Purimitla, S.R. Wake field studies of tidal current turbines with different numerical methods. *Ocean Eng.* **2016**, *117*, 383–397. [CrossRef]
36. Sánchez, S.; Hidalgo, V.; Velasco, M.; Puga, D.; López-Jiménez, P.A.; Sánchez, M.P. Parametric study of a horizontal axis wind turbine with similar characteristics to those of the Villonaco wind power plant. *J. Appl. Res. Technol. Eng.* **2021**, *2*, 51–62. [CrossRef]
37. Dehouck, V.; Lateb, M.; Sacheau, J.; Fellouah, H. Application of the BEM Theory to design HAWT blades. *J. Sol. Energy Eng.* **2017**, *104*, 014501-9.
38. Chen, Y.; Lin, B.; Lin, J.; Wang, S. Experimental study of wake structure behind a horizontal axis tidal stream turbine. *Appl. Energy* **2017**, *196*, 82–96. [CrossRef]
39. Mycek, P.; Gaurier, B.; Germain, G.; Pinon, G.; Rivoalen, E. Experimental study of the turbulence intensity effects on marine current turbines behaviour. Part II: Two interacting turbines. *Renew. Energy* **2014**, *68*, 876–892. [CrossRef]
40. Yamini, O.A.; Movahedi, A.; Mousavi, S.H.; Kavianpour, M.R.; Kyriakopoulos, G.L. Hydraulic Performance of Seawater Intake System Using CFD Modeling. *J. Mar. Sci. Eng.* **2022**, *10*, 988. [CrossRef]
41. Zhang, J.; Zhou, Y.; Lin, X.; Wang, G.; Guo, Y.; Chen, H. Experimental investigation on wake and thrust characteristics of a twin-rotor horizontal axis tidal stream turbine. *Renew. Energy* **2022**, *195*, 701–715. [CrossRef]
42. Moshfeghi, M.; Shams, S.; Hur, N. Aerodynamic performance enhancement analysis of horizontal axis wind turbines using a passive flow control method via split blade. *J. Wind. Eng. Ind. Aerodyn.* **2017**, *167*, 148–159. [CrossRef]
43. Tian, W.; Mao, Z.; Ding, H. Design, test and numerical simulation of a low-speed horizontal axis hydrokinetic turbine. *Int. J. Nav. Arch. Ocean Eng.* **2018**, *10*, 782–793. [CrossRef]
44. UIUC Applied Aerodynamics Group, Department of Aerospace Engineering. Available online: https://m-selig.ae.illinois.edu/ads/coord_database.html (accessed on 19 September 2021).
45. O'Brien, J.; Young, T.; O'Mahoney, D.; Griffin, P. Horizontal axis wind turbine research: A review of commercial CFD, FE codes and experimental practices. *Prog. Aerosp. Sci.* **2017**, *92*, 1–24. [CrossRef]
46. Lawson, M.J.; Li, Y.; Sale, D.C. Development and verification of a computational fluid dynamics model of a horizontal-axis tidal current turbine. In Proceedings of the ASME 2011 30th International Conference on Ocean, Offshore and Arctic Engineering, Rotterdam, The Netherlands, 19–24 June 2011; American Society of Mechanical Engineers: Rotterdam, The Netherlands, 2011; pp. 711–720. [CrossRef]
47. Tu, T.N. Numerical simulation of propeller open water characteristics using RANSE method. *Alex. Eng. J.* **2019**, *58*, 531–537. [CrossRef]
48. Lee, J.H.; Park, S.; Kim, D.H.; Rhee, S.H.; Kim, M.-C. Computational methods for performance analysis of horizontal axis tidal stream turbines. *Appl. Energy* **2012**, *98*, 512–523. [CrossRef]